Biomedical Optics EXPRESS

Non-contact photoacoustic imaging using a fiber based interferometer with optical amplification

Armin Hochreiner,[1,*] Johannes Bauer-Marschallinger,[1] Peter Burgholzer,[1] Bernhard Jakoby,[2] and Thomas Berer[1]

[1]*Research Center for Non-Destructive Testing GmbH (RECENDT), Altenberger Straße 69, 4040 Linz, Austria*
[2]*Institute for Microelectronics and Microsensors, Johannes Kepler University Linz, Altenberger Straße 69, 4040 Linz, Austria*
[*]*armin.hochreiner@recendt.at*

Abstract: In photoacoustic imaging the ultrasonic signals are usually detected by contacting transducers. For some applications contact with the tissue should be avoided. As alternatives to contacting transducers interferometric means can be used to acquire photoacoustic signals remotely. In this paper we report on non-contact three and two dimensional photoacoustic imaging using an optical fiber-based Mach-Zehnder interferometer. A detection beam is transmitted through an optical fiber network onto the surface of the specimen. Back reflected light is collected and coupled into the same optical fiber. To achieve a high signal/noise ratio the reflected light is amplified by means of optical amplification with an erbium doped fiber amplifier before demodulation. After data acquisition the initial pressure distribution is reconstructed by a Fourier domain reconstruction algorithm. We present remote photoacoustic imaging of a tissue mimicking phantom and on chicken skin.

OCIS codes: (170.5120) Photoacoustic imaging; (120.0280) Remote sensing and sensors; (110.2350) Fiber optics imaging; (140.4480) Optical amplifiers; (110.7170) Ultrasound; (170.1470) Blood or tissue constituent monitoring; (120.3180) Interferometry.

References and links

1. L. V. Wang and S. Hu, "Photoacoustic tomography: in vivo imaging from organelles to organs," Science **335**(6075), 1458–1462 (2012).
2. G. Rousseau, B. Gauthier, A. Blouin, and J.-P. Monchalin, "Non-contact biomedical photoacoustic and ultrasound imaging," J. Biomed. Opt. **17**(6), 061217 (2012).
3. V. Ntziachristos, J. S. Yoo, and G. M. van Dam, "Current concepts and future perspectives on surgical optical imaging in cancer," J. Biomed. Opt. **15**(6), 066024 (2010).
4. E. Z. Zhang, J. G. Laufer, R. B. Pedley, and P. C. Beard, "In vivo high-resolution 3D photoacoustic imaging of superficial vascular anatomy," Phys. Med. Biol. **54**(4), 1035–1046 (2009).
5. B. P. Payne, V. Venugopalan, B. B. Mikić, and N. S. Nishioka, "Optoacoustic tomography using time-resolved interferometric detection of surface displacement," J. Biomed. Opt. **8**(2), 273–280 (2003).
6. S. A. Carp, A. Guerra III, S. Q. Duque, Jr., and V. Venugopalan, "Optoacoustic imaging using interferometric measurement of surface displacement," Appl. Phys. Lett. **85**(23), 5772–5774 (2004).
7. S. A. Carp and V. Venugopalan, "Optoacoustic imaging based on the interferometric measurement of surface displacement," J. Biomed. Opt. **12**(6), 064001 (2007).
8. Y. Hou, S. W. Huang, S. Ashkenazi, R. Witte, and M. O'Donnell, "Thin polymer etalon arrays for high-resolution photoacoustic imaging," J. Biomed. Opt. **13**(6), 064033 (2008).
9. J. D. Hamilton and M. O'Donnell, "High frequency ultrasound imaging with optical arrays," IEEE Trans. Ultrason. Ferroelectr. Freq. Control **45**(1), 216–235 (1998).
10. E. Zhang, J. Laufer, and P. Beard, "Backward-mode multiwavelength photoacoustic scanner using a planar Fabry-Perot polymer film ultrasound sensor for high-resolution three-dimensional imaging of biological tissues," Appl. Opt. **47**(4), 561–577 (2008).
11. Y. Wang, C. Li, and R. K. Wang, "Noncontact photoacoustic imaging achieved by using a low-coherence interferometer as the acoustic detector," Opt. Lett. **36**(20), 3975–3977 (2011).
12. T. Berer, A. Hochreiner, S. Zamiri, and P. Burgholzer, "Remote photoacoustic imaging on solid material using a two-wave mixing interferometer," Opt. Lett. **35**(24), 4151–4153 (2010).

#194856 - $15.00 USD Received 29 Jul 2013; accepted 23 Sep 2013; published 2 Oct 2013

13. A. Hochreiner, T. Berer, H. Grün, M. Leitner, and P. Burgholzer, "Photoacoustic imaging using an adaptive interferometer with a photorefractive crystal," J Biophotonics **5**(7), 508–517 (2012).
14. G. Rousseau, A. Blouin, and J.-P. Monchalin, "Non-contact photoacoustic tomography and ultrasonography for tissue imaging," Biomed. Opt. Express **3**(1), 16–25 (2012).
15. S. Krishnaswami, "Theory and applications of laser-ultrasonic techniques" in Ultrasonic Nondestructive Evaluation: Engineering and Biological Material Characterization, pp. 435–494, CRC Press, 2003.
16. J. Bauer-Marschallinger, K. Felbermayer, A. Hochreiner, H. Grün, G. Paltauf, P. Burgholzer, and T. Berer, "Low-cost parallelization of optical fiber based detectors for photoacoustic imaging," Proc. SPIE **8581**, 85812M, 85812M-8 (2013).
17. L. J. Busse, "Three-dimensional imaging using a frequency-domain synthetic aperture focusing technique," IEEE Trans. Ultrason. Ferroelectr. Freq. Control **39**(2), 174–179 (1992).
18. M. Jaeger, D. Birtill, A. Gertsch, E. O'Flynn, and J. Bamber, "Clinical demonstration of epi-mode photoacoustic clutter reduction using palpation scanning," 2011 IEEE International Ultrasonics Symposium (IUS), 2360–2363 (2011).
19. M. Jaeger, D. Harris-Birtill, A. Gertsch, E. O'Flynn, and J. Bamber, "Deformation-compensated averaging for clutter reduction in epiphotoacoustic imaging *in vivo*," J. Biomed. Opt. **17**(6), 066007 (2012).
20. American National Standard for the Safe Use of Lasers, ANSI Z136.1–2007, Laser Institute of America, Orlando, FL (2007).
21. E. Z. Zhang, B. Povazay, J. Laufer, A. Alex, B. Hofer, B. Pedley, C. Glittenberg, B. Treeby, B. Cox, P. Beard, and W. Drexler, "Multimodal photoacoustic and optical coherence tomography scanner using an all optical detection scheme for 3D morphological skin imaging," Biomed. Opt. Express **2**(8), 2202–2215 (2011).
22. L. Li, K. Maslov, G. Ku, and L. V. Wang, "Three-dimensional combined photoacoustic and optical coherence microscopy for in vivo microcirculation studies," Opt. Express **17**(19), 16450–16455 (2009).
23. S. Jiao, M. Jiang, J. Hu, A. Fawzi, Q. Zhou, K. K. Shung, C. A. Puliafito, and H. F. Zhang, "Photoacoustic ophthalmoscopy for in vivo retinal imaging," Opt. Express **18**(4), 3967–3972 (2010).
24. X. Zhang, H. F. Zhang, and S. Jiao, "Optical coherence photoacoustic microscopy: accomplishing optical coherence tomography and photoacoustic microscopy with a single light source," J. Biomed. Opt. **17**(3), 030502 (2012).

1. Introduction

Photoacoustic Imaging (PAI) is a non-invasive imaging modality which allows structural, functional and molecular imaging [1]. Imaging relies on the photoacoustic effect, which describes conversion between light and acoustic waves due to absorption of electromagnetic waves and localized thermal expansion. In practice, short pulses of electromagnetic radiation, mostly short laser pulses, are used to illuminate a sample. The local absorption of the light is followed by rapid heating, which subsequently leads to thermal expansion and the generation of broadband acoustic waves. By recording the generated ultrasonic waves the initial absorbed energy distribution can be assessed. Thus, photoacoustic imaging is a hybrid technique making use of optical absorption and ultrasonic wave propagation leading to high contrast and high spatial resolution, respectively.

To record the ultrasonic waves, in PAI usually piezoelectric transducers are used. For acoustic coupling between specimen and transducer an adequate coupling medium has to be used (e.g. water or ultrasound gel). While this is no major limitation for many applications, there are cases where contacting means should be avoided, e.g. in burn diagnostics [2] or for in-line material inspection. For inter-operative imaging contacting transducers hinder the surgery. Furthermore, for many kinds of surgery contacting means are prohibited, e.g. in brain surgery [3]. As an alternative to piezoelectric transducers interferometric detection schemes have been reported as a means to acquire the ultrasonic signals [4–11]. These techniques, however, still demand direct contact with the tissue, immersion in water, or at least a liquid layer on top of the sample. Non-contact, or remote, photoacoustic imaging, where no coupling agent is required was demonstrated for industrial materials in 2010 [12] and recently also for biological samples [2, 13, 14]. In these works the motion of a surface was measured remotely by means of interferometry.

In this paper, photoacoustic signals are acquired by using an enhanced Mach-Zehnder interferometer with optical amplification, whereby the major part of the interferometer is realized in a fiber optic network. The fiber optics allows a simple, compact, and flexible system and the Mach-Zehnder setup permits high frequency detection only limited by the

#194856 - $15.00 USD Received 29 Jul 2013; accepted 23 Sep 2013; published 2 Oct 2013

detection electronics. As detection laser we use a low-power laser source with an eye-safe wavelength of 1550 nm. To achieve a high signal/noise rate the reflected light is amplified by means of optical amplification with an erbium doped fiber amplifier (EDFA) before demodulation.

The paper is constructed as follows. In section 2 we describe the experimental setup and the detection principle. Experimental results obtained on a tissue mimicking phantom and on a chicken thigh are presented in section 3. In section 4 we discuss laser safety, the minimum detectable pressure, system noise and give an outlook.

2. Experimental setup

2.1 Detection principle

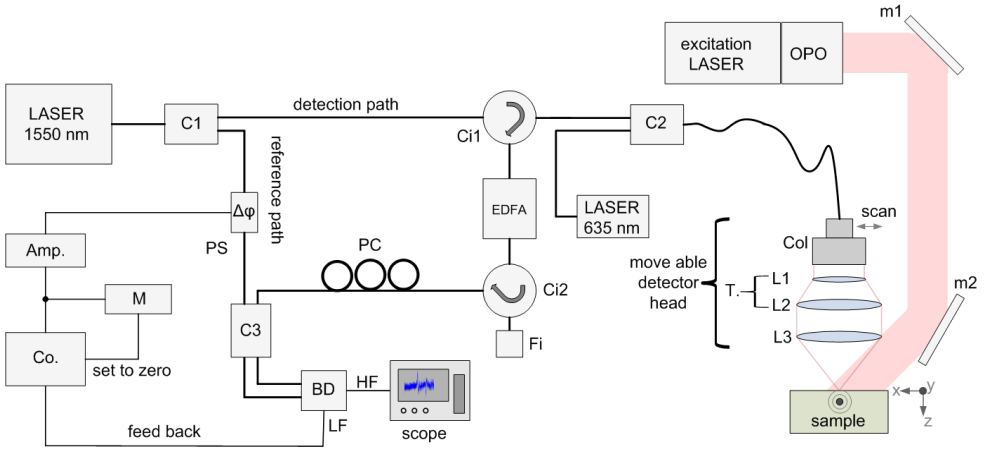

Fig. 1. Schematic of the remote photoacoustic imaging setup (see text).

In Fig. 1 a schematic of the remote photoacoustic setup (rPAI) is illustrated. For detecting the photoacoustic waves a fiber based Mach-Zehnder interferometer (MZI) is used. As optical fibers we use SMF-28e fibers which are the standard type for the used wavelength of 1550 nm. As detection laser, i.e. the optical source of the interferometer, we use a low bandwidth cw fiber laser (Koheras AdjustiK) with a central wavelength of 1549.9 nm, linewidth <3 kHz and maximum output power of 25 mW. The wavelength of the laser can be shifted ± 250 pm by thermal tuning. Light of the detection laser is split into a detection path and a reference path using an 80/20 splitter (C1). The major part, i.e. the detection beam, is directed to the sample surface via a circulator (Ci1), a 99/1 coupler (C2), a fiber collimator with collimated beam diameter of 7mm (Col), and a lenses system consisting of a telescope (L1, L2, magnification 2x) and a 2" achromatic front lens (L3, f = 75 mm) for focusing the detection beam on the surface of the sample. The detector head consists of the collimator and the lense system L1-L3 and is mounted on two linear stages (Physik Instrumente M-413.22S). An aiming laser at a visible wavelength of 635 nm is coupled by the 1% input of coupler C2 into the detector head to simplify adjustment of the detection beam.

Light which is back reflected from the surface of a specimen is collected by the detector head and coupled into the single mode fiber. The power of the collected light depends on the measured surface and is typically less than 1‰ of the incident light power. To increase the power level, the weak beam is directed to an erbium doped fiber amplifier (EDFA, Ericsson PGE-608-30-PA) by circulator Ci1. EDFAs exhibit broad band noise due to amplified spontaneous emission (ASE). The ASE noise spectrum is approximately the same as the gain spectrum of the amplifier, i.e. for our device 1528 nm to 1563 nm. To reduce ASE we use a small bandwidth filter (Fi, 0.25 nm at full with half maximum (FWHM)) in a reflection configuration. The detection laser is thermally tuned to the center wavelength of the filter

#194856 - $15.00 USD Received 29 Jul 2013; accepted 23 Sep 2013; published 2 Oct 2013

(1550.12 nm). The filter reflects only the central wavelength region and is thereby removing the major part of the ASE spectrum from the system. A circulator, Ci2, directs the filtered and reflected light to a polarization controller (PC). As no polarization maintaining fibers are used in the setup, mechanical stresses within the fibers lead to birefringence and consequently to a change in the polarization state. In order to optimize the interference of the light the polarization state of the two light paths has to be matched. This is done with the polarization controller. Reference path and detection path are combined by a 50/50 coupler (C3) and brought to interference. The modulated light intensity is then converted into electrical signals by a self-built balanced photo detector (BD). The detector offers two outputs, one for high frequencies (HF) and one for low frequencies (LF). The high frequency output is sampled with an 8-bit digital scope (LeCroy WaveRunner 44Xi-A). The low frequency output is coupled to a self-built analog controller (Co). To ensure the best sensitivity, the interferometer is stabilized in the quadrature point, i.e. in the point with highest slope, of the interferometer. The output of the controller is amplified by a high voltage amplifier connected to a piezoelectric phase shifter ($\Delta\varphi$) with an monitoring circuit (M). Fast vibrations on the sample surface change the relative phase between reference and sample beam, thus the high-frequency output of the photodetector is directly related to the surface displacements. By excitation of photoacoustic signals with an excitation laser and recording the time traces of the displacements on different locations on the sample the initial pressure distribution can be assessed.

In general the fiber based MZI offers greater flexibility and a simpler setup compared to free-space optics. As only few optical lenses are used the system is less sensitive to contaminations like dust. Using components as usually used in telecommunication industries guarantees long life times and relatively low costs.

2.2 Power levels and optical amplification

In the experiments two different samples were examined, a tissue mimicking phantom with a polymer surface and a chicken thigh phantom. For the tissue mimicking phantom the detection laser power was set to 5.3 mW at the collimator; the power in the reference arm was measured to be 1mW. For the chicken phantom the respective power levels were 8 mW at the collimator and 1.5 mW in the reference arm. Power levels of the reflected light measured after the circulator were found to be 4.6 µW and 1.2 µW for the polymer and chicken skin surface, respectively. The shot noise limited signal/noise ratio (SNR) of the interferometer is dependent on the powers in the reference path and signal path [15]. To compensate for the high losses we amplify the reflected light in the signal path by means of optical amplification. The used EDFA has an input signal range from −40 dBm to −10 dBm, i.e. 0.1 µW to 100 µW, and a nominal amplification of 28 dB at −30 dBm. The returned power levels lie within the specified input level range. However, we found the amplification to be higher than specified, i.e. above 30 dB, for input levels between 0.5 µW and 8 µW. The power levels in the signal path measured after the filter and circulator, Ci2, were found to be 5 mW and 1.6 mW, for the polymer and chicken skin samples. A detailed discussion on the minimal detectable pressure is presented in section 4.2.

2.3 Detection electronics and controller

The high frequency output of the balanced photo detector, described in detail in [16], has a −3 dB bandwidth of 45 MHz, a gain of 97 dB at 10 MHz and is used for acquisition of the photoacoustic signals. To prevent the high gain amplifier from saturation due to low frequency disturbances, e.g. acoustic noise in the lab, an active low-pass filter feedback loop is employed. The low frequency output of the detector has lower gain. Due to the lower gain of the LF output the detector does not saturate at the power levels used in the present paper.

For stabilization of the working point we use a self-built analog proportional-integral-controller built with operational amplifiers. The controller keeps the interferometer at the

#194856 - $15.00 USD Received 29 Jul 2013; accepted 23 Sep 2013; published 2 Oct 2013

quadrature point by applying a voltage to phase shifter (Δφ) so that the low-frequency output of the BD is zero. As the setup consists of a long fiber optic network thermal drifts can occur, especially in the EDFA. If the drifts become too large, i.e. if the maximum tuning range of the phase shifter is reached, the controller cannot operate anymore. To prevent this, a monitoring circuit (M) measures the output level of the controller and resets the controller when the levels are too high.

2.4 Optical excitation

To generate ultrasound waves within the sample pulses from an optical parametric oscillator (OPO, Continuum Surelite OPO Plus) are used. The OPO is pumped at a wavelength of 532 nm provided by a frequency double Nd:YAG laser with a center wavelength of 1064 nm (Continuum Surelite SL I-20) at 20 Hz repetition rate. The pump laser has a maximum energy of 450 mJ (at 1064 nm) per pulse and nominal pulse length of 4-7 ns. The OPO can provide excitation wavelengths between 680 nm and 900 nm. The maximum pulse energy (depending on the used wavelength) after the OPO is 70 mJ at a pulse length of 3-5 ns and a beam diameter of 12 mm. The excitation beam is guided to the sample by a mirror system, indicated by mirrors m1 and m2 in Fig. 1. The excitation spot on the sample has an elliptical shape with major axis of 17 mm and 12 mm.

2.5 Measurement and image reconstruction

For photoacoustic imaging ultrasonic signals are acquired on different locations on the surface of a specimen by scanning of the detector head. For scanning two linear stages were used. A self-written program which is executed on the digital scope is used to control the stages and the scope, and to store the acquired data to a hard disk. An additional self-made stage with a stepper motor, also controllable with the software, is used to find the focus on the sample surface. Data acquisition is done with the 8-bit digital scope featuring a maximum bandwidth of 400 MHz. Although the balanced photodetector has a −3dB bandwidth of 45 MHz we limited the bandwidth of the scope to 20 MHz to reduce noise and increase SNR. The bandwidth is, however, high enough to resolve the smallest features in the phantoms with diameters of 300 µm.

After the measurements a reconstruction algorithm is applied to recover the two or three dimensional image of the initial pressure distribution. For image reconstruction we use a Fourier domain synthetic aperture focusing technique (FSAFT) [17]. This algorithm is commonly used for pulse-echo measurements, but can also be used for single transmission measurements. In the first case the sound velocity for the reconstruction is set to half of the velocity in the medium; in the latter (our) case simply the sound velocity has to be used. As pointed out in [12] the interferometer measures the out-of-plane displacements on the specimen's surface and not the pressure. Therefore, the 1st derivative in time of the data is calculated and used for reconstruction. After reconstruction a Hilbert transform is applied to the reconstructed data set.

3. Experiments

3.1 Three-dimensional measurement of tissue mimicking phantom

In Fig. 2 the schematic of the phantom is illustrated. The sample consists of a silicone tube filled with black ink (Pelikan 4001 brillant black). The tube is formed to a knot and immersed in a tank made of acrylic glass filled with a milk/water emulsion. The tube has an outer diameter and an inner diameter of 600 µm and 300 µm, respectively. Milk was diluted into the water to increase optical scattering in order to provide homogeneous illumination of the sample as it is the case in tissue. As detection surface an adhesive tape was used to mimic smooth skin. The tape was fixed on an acrylic glass tube and immersed in the solution.

#194856 - $15.00 USD Received 29 Jul 2013; accepted 23 Sep 2013; published 2 Oct 2013

The generated ultrasound waves were acquired by the MZI setup on the air/adhesive-tape interface. The power of the detection laser was set to 5.3 mW. For excitation a wavelength of 740 nm and a radiant exposure of 105 Jm^{-2} were used.

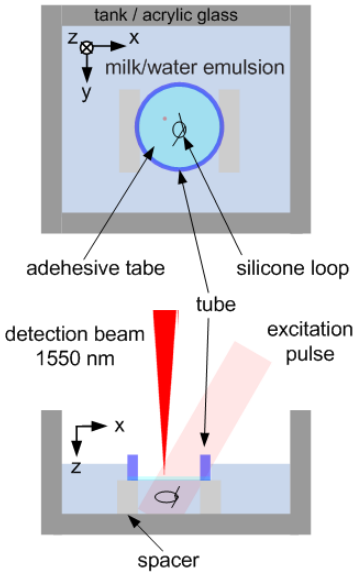

Fig. 2. Schematic of the sample consisting of knotted silicone tube filled with black ink. The tube has an outer diameter and an inner diameter of 600 µm and 300 µm, respectively. The loop is immersed in a tank filled with a milk/water emulsion.

For acquiring a three dimensional data set, the sample surface was scanned in two dimensions by raster scanning in *x* and *y*-direction with 81 steps and 71 steps, respectively. The step size was chosen with 100 µm in both directions, about three times smaller than the inner diameter of the silicone tube, leading to a total scan area of 8 × 7 mm^2. Data were acquired without averaging.

Figures 3(a)-3(c) show the maximum amplitude projections of the reconstructed image along *z*-, *x*-, and *y*-direction, respectively. For image reconstruction a FSAFT algorithm was used. The colorbar shown beside Fig. 3(b) belongs to all three projection images. In Fig. 3(d) a photograph of the ink-filled loop after the measurement is depicted for comparison. In general the reconstructed images reproduce the shape and size of the object well. We found the brighter parts in Fig. 3(a) to have a diameter of approximately 300 µm which fits the inner diameter of the tube. The brighter areas are surrounded by somewhat darker areas. The diameter of these areas was measured to be around 600 µm. This corresponds to the outer diameter of the tubes. However, we did not find significant photoacoustic signals when measuring a silicone tube filled with water only. We repeated the measurement with an empty silicone tube which was immersed in ink overnight and observed weak photoacoustic signals. We therefore think that part of the ink diffused into the silicone tube and is responsible for the photoacoustic signals obtained from silicone tube. The brightness of the features decreases with increasing depth *z*. We think this is due to absorption of the excitation light in the milk/water solution. Also the reconstructions show some discontinuities. For example in Fig. 3(a) such a discontinuity is located at the crossing at $x = 6$ mm, $y = 2$ mm. From Fig. 3(b) we can see that this part is shadowed by the overlying structure at $z = 4$ mm. Another discontinuity can be identified in Fig. 3(b) at $y = 5$ mm, $z = 2.5$ mm. From Fig. 3(a) we see this part is shadowed by the structure crossing at $x = 2$ mm. We therefore think that these discontinuities are mainly due to optic and acoustic shadowing of deep lying structures by structures lying above.

#194856 - $15.00 USD Received 29 Jul 2013; accepted 23 Sep 2013; published 2 Oct 2013

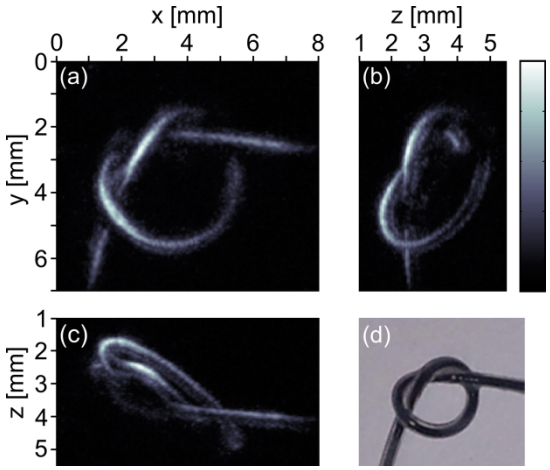

Fig. 3. (a)-(c) Maximum intensity projections of a silicone loop filled with ink along the *z*-, *x*-, and *y*-direction, respectively. Data were acquired by single-shot measurements, i.e. without averaging. (d) Photograph of the ink-filled tube taken after the measurement.

3.2 Two-dimensional measurement on chicken skin

For many applications a B-scan is sufficient to estimate the depths of features, e.g. blood vessels, from the reconstructed two-dimensional image. Thereby the amount of measurement points is largely reduced and consequently also the measurement time. To demonstrate two-dimensional imaging for biomedical applications we choose a more realistic phantom. We selected a chicken thigh and removed the cutis on an area of 15 mm × 15 mm with a scalpel. Subsequently, ultrasound gel was applied on the muscle tissue and two artificial blood vessels, i.e. two parallel running tubes filled with black ink (Pelikan 4001 brillant black), were placed into the gel. Afterwards, the cutis was placed back above the structure.

A B-scan was acquired by measuring 201 points in *x*-direction on a length of 6 mm. For comparison the measurement was repeated by recording three B-scans separated by 30 µm in *y*-direction. For all measurements the probe beam was set to 8 mW and photoacoustic signals were acquired without averaging.

The reconstructed initial pressure distribution for the B-scan is shown in Fig. 4(a). The two ink-filled silicon-tubes can be clearly identified. Figure 4(b) shows the maximum intensity plot of the reconstruction from the three line scans. Here the artificial blood vessels appear a bit more defined. In both reconstructions a strong background noise is observed. This background noise may be due to clutter which is usually observed in tissue samples when measuring in the so called epi-mode, i.e. when exciting the sample through the same tissue surface where ultrasound is detected. The clutter emerges from photoacoustic transients generated in the bulk tissue outside the image plane (bulk clutter) [18, 19].

#194856 - $15.00 USD Received 29 Jul 2013; accepted 23 Sep 2013; published 2 Oct 2013

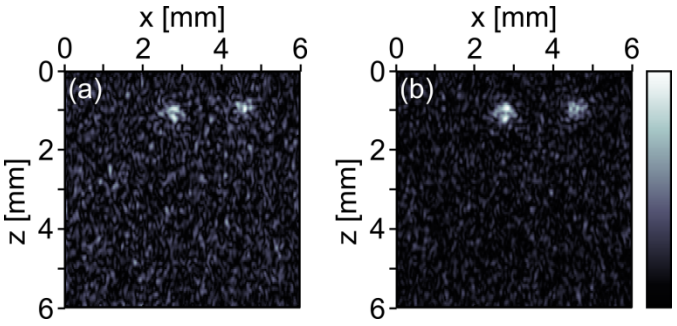

Fig. 4. Photoacoustic images of two ink-filled silicon tubes in chicken thigh. The photoacoustic signals were acquired on the chicken skin without averaging. (a) Reconstruction from a line scan with 201 points. (b) Maximum intensity projection from three line scans with 201 × 3 points. The colorbar belongs to both images.

Examination of the chicken skin after the measurement showed no signs of skin damage or burns. These results demonstrate the potential of our technique for non-contact photoacoustic imaging in biomedical applications.

4. Discussion and outlook

4.1 Laser safety

The used detection wavelength, λ, of 1550 nm lies within the eye-safe wavelength range where the cornea and lens absorbs the light. The MPE (maximum permissible exposure) for cornea and skin at this wavelength is 10^4 Jm^{-2} for exposure times between 1ps and 10s, and 1000 Wm^{-2} for exposure times greater than 10 s [20]. After the collimator the beam has a diameter of 7 mm; the maximum power used in the experiments was 8 mW. This leads to a radiant exposure of approximately 200 Wm^{-2} after the collimator which is below the MPE. Therefore, no laser safety glasses are needed.

When the beam is focused onto a specimen the intensity increases by several orders of magnitude. In the presented setup the beam is expanded by a factor of two by a telescope before focused on the surface with a lens with a focal length, f_L, of 75 mm. The minimum diameter at the surface, d_s, is then given by

$$d_S = 4\frac{\lambda f_L M^2}{\pi d_C}, \tag{1}$$

where M^2 is the quality factor of the beam (1.0 for an ideal Gaussian beam) and d_c is the diameter of the beam before the focusing lens. This results in a minimum spot diameter of 10.5 µm. Although, we do not suppose that we reach this lower limit we use this value for further calculations. For single shot measurements with 20 Hz and a maximum power of 8 mW we find the intensity per measurement point to be about 4.6×10^6 Jm^{-2}, which is two orders of magnitude above the allowed MPE. To minimize laser exposure a special tailored long pulse laser with a pulse length of about 25 µs was used by Rousseau et al. [2, 14]; in [13] the detection laser was pulsed to minimize exposure. In a future version of the presented setup we plan to use an intensity modulator to switch the probe beam on only during the measurement. The maximum acquired signal length in this paper was 10 µs. By turning on the detection laser only for this time span the exposure for a single shot measurement would reduce to 920 Jm^{-2} which is more than one order of magnitude below the MPE. In this case another stabilization scheme using digital controllers has to be used. Laser intensities could be further reduced by increasing the spot diameter. For the used bandwidth of 20 MHz a spot diameter of 50 µm would be sufficient. By increasing the beam diameter and pulsing the

#194856 - $15.00 USD Received 29 Jul 2013; accepted 23 Sep 2013; published 2 Oct 2013

laser, the exposure would reduce to 40 Jm^{-2}. Without pulsing, however, the exposure would be 2.0×10^5 Jm^{-2}, which is still one order of magnitude above the MPE.

The radiant exposures for excitation were 105 Jm^{-2} at 740 nm for the tissue mimicking phantom and 220 Jm^{-2} at 760 nm for the chicken phantom. The MPE for the used wavelengths are 240 Jm^{-2} and 260 Jm^{-2}, respectively. Thus both measurements were done below the MPE. As the excitation spot and the detection spot overlap their MPE cannot be considered separately. Overlapping can be avoided by a using masking illumination scheme where the area around the detection spot is masked, as demonstrated in [2, 14]. The other solution to avoid too high exposure is to reduce the radiation of the detection laser by using the pulsed detection scheme as described above.

4.2 Minimum detectable pressure

The shot-noise limited sensitivity, i.e. the minimum detectable displacement u_{min} on the sample surface, of our interferometer depends on the powers in the reference path, P_{ref}, and signal path, P_{sig} [15]:

$$u_{\min} = \frac{1}{k_{opt} M_i} \sqrt{\frac{h\nu B}{\eta (P_{sig} + P_{ref})}}, \tag{2}$$

where k_{opt} is the optical wave number, h the Planck's constant, ν the optical frequency, B the detection bandwidth, η the detector quantum efficiency and M_i is the modulation depth the interferometer is given as

$$M_i = \frac{2\sqrt{P_{ref} \cdot P_{sig}}}{P_{ref} + P_{sig}}. \tag{3}$$

The shot-noise limit is the fundamental physical limit when all other sources of noise are eliminated. From the minimum detectable displacements we can find the minimum detectable pressure p_{min} by [14]:

$$p_{\min} = \pi Z u_{\min} f, \tag{4}$$

where Z is the acoustic impedance of the specimen, typically about 1.5×10^6 Pa·s/m for biological tissue or water, and f is the ultrasonic frequency. For the tissue mimicking phantom we found the power in the reference path and signal path after amplification to be 1 mW and 5 mW, respectively. With the spectral responsivity $R_\lambda = \eta e/(h\nu)$ of the used photodiodes of 0.95 A/W, the used detection bandwidth of 20 MHz and setting the typical ultrasonic frequency to half the bandwidth we find the minimum detectable pressure to be 275 Pa. For many measurements a lower bandwidth would be sufficient. From Eq. (2) and (4) we see that the minimum detectable pressure is proportional to $B^{3/2}$. For an ultrasonic bandwidth of 5 MHz the minimum detectable pressure reduces to 35 Pa. The sensitivity could be further improved by optimizing the splitting ratio of reference and signal path and obviously by a using higher detection power. For the chicken skin phantom we found the powers to be 1.5 mW and 1.6 mW in the reference and signal path, respectively. For a bandwidth of 20 MHz we get a minimum detectable pressure in the shot-noise limit of 380 Pa. For the bandwidth of 5 MHz the detectable pressure reduces to about 50 Pa. Anyhow, we do not claim to have reached the shot-noise limit with the present setup. A detailed noise analysis will be object of future works.

4.3 Noise and ASE

The main source of noise in EDFAs is ASE. To reduce noise in our system we included a small bandwidth filter. We found that the system noise decreases with decreasing bandwidth

#194856 - $15.00 USD Received 29 Jul 2013; accepted 23 Sep 2013; published 2 Oct 2013

of the filter and conclude that the main source of noise in our system is ASE. Such filters are typically used in communications systems to multiplex or demultiplex different channels. Today's DWDM (dense wavelength division multiplexing) systems have a channel spacing of 100 GHz or 50 GHz, i.e. 0.8 nm and 0.4 nm, respectively. The −3 dB bandwidth of a typical DWDM filter with channel spacing 50 GHz is between 0.2 nm and 0.3 nm. In the presented setup we use a filter exhibiting a −3 dB bandwidth of 0.25 nm. Technology is moving toward 25 GHz or even 12.5 GHz spacing. The according −3 dB bandwidths of these filters are 0.1 nm and 0.05 nm, respectively. Using such a filter may further reduce ASE in our system and will help to bring the system towards the shot noise limit.

4.4 Outlook

Using optical fibers offers various advantages. Some of these, like the great flexibility, the relatively simple setup or the reliability of the fiber optic components have been mentioned before. Moreover, the single mode fiber delivery allows the fabrication of a small footprint photoacoustic endoscope. As the presented technique works without the aid of a coupling medium, also regions without the presence of body fluids, e.g. the esophagus, could be imaged. The fiber optic assembly also allows combination with other fiber based imaging techniques, e.g. with optical coherence tomography (OCT). Combinations of OCT with PAI have been recently demonstrated [11, 21–24]. However, with exception of reference [11], these methods rely on contacting transducers. Thus, these approaches do not make full use of the remote nature of OCT, therefore limiting the applicability of the combined setups. This limitation could be overcome by combining OCT with the presented non-contact photoacoustic imaging system.

5. Conclusion

We reported on non-contact photoacoustic imaging using a Mach-Zehnder interferometer with optical amplification. Ultrasonic signals were recorded on the surface of a specimen remotely by means of interferometry. As the backscattered and collected light intensity is low, the light was amplified using an optical amplifier before demodulation. For imaging, the detector head was raster scanned and photoacoustic signals were recorded on different locations on the sample surface. After acquisition the derivative in time was calculated and the initial pressure distributing was reproduced using an F-SAFT algorithm.

We showed three-dimensional measurements on a tissue mimicking phantom consisting of a silicon tube filled with ink immersed in a milk/water emulsion and a polymer surface. The three dimensional shape of the tube and its size could be reproduced well. For many applications two-dimensional images are sufficient. Two-dimensional imaging was demonstrated on a chicken thigh phantom by recording line scans on chicken skin.

Additionally we addressed lasers safety, system noise, and the minimum detectable pressure. Even as the sensitivity is lower than that of state of the art piezoelectric transducers, the advantages of a non-contact method may be beneficial for many applications.

Acknowledgments

This work has been supported by the Austrian Science Fund (FWF), project numbers P25584-N20 and S10503-N20, the European Regional Development Fund (EFRE) in the framework of the EU-program Regio 13, and the federal state Upper Austria.